*J. Fluid Mech.* (2025), *vol.* 1009, A6, doi:10.1017/jfm.2025.179

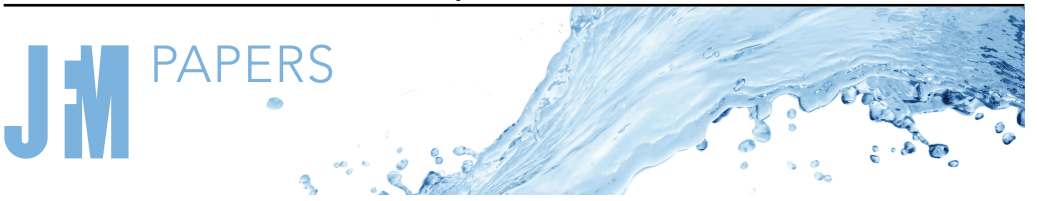


# Pressure-driven flow through superhydrophobic pipes with general patterns of longitudinal no-shear stripes

**Sebastian Zimmermann**[1], **Clarissa Schönecker**[1] **and Darren G. Crowdy**[2]

[1]Rheinland-Pfälzische Technische Universität Kaiserslautern-Landau (RPTU), D-67663 Kaiserslautern, Germany

[2]Department of Mathematics, Imperial College London, 180 Queen's Gate, London SW7 2AZ, UK

**Corresponding author**: Darren G. Crowdy, d.crowdy@imperial.ac.uk

(Received 20 September 2024; revised 19 December 2024; accepted 2 February 2025)

Analytical expressions are derived for the velocity field, and effective slip lengths, associated with pressure-driven longitudinal flow in a circular superhydrophobic pipe whose boundary is patterned with a general arrangement of longitudinal no-shear stripes not necessarily possessing any rotational symmetry. First, the flow in a superhydrophobic pipe with $M$ different no-shear stripes in general position is found for $M = 1, 2, 3$. The method, which is based on use of so-called prime functions, is such that with these cases covered, generalisation to any $M \geqslant 1$ follows in a straightforward manner. It is shown how any one of these solutions can be generalised to solve for flow along superhydrophobic pipes where that pattern of $M$ menisci is repeated $N \geqslant 1$ times around the boundary in a rotational symmetric arrangement. The work provides an extension of the canonical pipe flow solution for an $N$-fold rotationally symmetric pattern of no-shear stripes due to Philip (*Angew. Math. Phys.*, vol. 23, 1972, pp. 353–372). The novel solution method, and the solutions that it produces, have significance for a wide range of mixed boundary value problems involving Poisson's equation arising in other applications.

**Key words:** drag reduction, pipe flow, microfluidics

## 1. Introduction

The study of superhydrophobic surfaces (SHS) has attracted considerable interest in recent years, as they promise reduced resistance for liquid motion along surfaces, a feature of great importance for many engineering applications (Rothstein 2010; Wang *et al.* 2020;

Liravi *et al.* 2020). The effect and functionality of SHS are decisively based on their ability to entrap air in surface roughness, and to maintain the so-called Cassie state (Cassie & Baxter 1944) where almost shear-free fluid–fluid interfaces displace parts of the no-slip solid wall. This phenomenon allows fluids to partially slip along these heterogeneous surfaces, while simultaneously reducing the wall surface fraction, the net effect being a reduction in viscous drag on a pressure-driven fluid. However, this desired effect is crucially dependent on the mobility of the interface. Studies have shown that the presence and deposition of surfactants and/or other impurities may hinder this very mobility, potentially leading to reduced slip or full loss of functionality (Song *et al.* 2018).

Nevertheless, the shear-free idealisation has by now established its place as an important baseline case: the theoretical analysis of SHS is typically based on the assumption that the shear stress tangential to the fluid–fluid interface, and the flow velocity normal to it, both vanish. This means that these shear-free interfaces do not pose any resistance for a liquid moving past them (Davis & Lauga 2009; Schönecker & Hardt 2015; Schnitzer & Yariv 2019). Analytical modelling of SHS is therefore primarily concerned with solving no-slip/no-shear mixed-type boundary value problems in various geometrical configurations. An early and important contribution to the theoretical understanding of such surfaces was made by Philip (1972), who derived several analytical solutions subject to these mixed boundary conditions using complex analysis techniques. Although originally intended to describe flow through and along porous media, these analytical models have become fundamental for SHS research. They cover a range of different cases, including flow along a single plate or between two infinite plates, and axial flow in circular pipes, each featuring either a single or periodic array of no-shear regions running longitudinally or transverse to the flow direction on otherwise no-slip solid walls.

Subsequent research has significantly expanded upon Philip's work. Lauga & Stone (2003) were the first to recognise the relevance of his solutions for modelling SHS, presenting them in a more tangible notation. They also derived an analytical model for a flow through SHS pipes containing transverse rather than longitudinal shear-free stripes, and have derived the effective slip length for both kinds of slippery pipes. The latter is a critical parameter for characterising and quantifying the overall degree of slip, achieved by averaging and uniformly smearing out the sum of all locally induced slippage onto the respective surface. The result is an intrinsic material property dependent on the functional morphology, which can be used as a boundary condition in numerical simulations and has therefore been widely studied to optimise SHS in practical applications (Lauga & Stone 2003; Tsai *et al.* 2009; Asmolov, Nizkaya & Vinogradova 2018). Further extensions include the study of protruded fluid–fluid interfaces in planar channels (Sbragaglia & Prosperetti 2007; Crowdy 2010, 2016, 2017), partially invaded cavities (Crowdy 2021*a*), superhydrophobic annular pipes (Crowdy 2021*b*), and the incorporation of non-zero interface shear stress (Belyaev & Vinogradova 2010; Schönecker & Hardt 2013; Schönecker *et al.* 2014; Zimmermann & Schönecker 2024), which additionally allows for the analytical modelling of liquid-infused surfaces.

Another extension of Philip's work, one that is closed related to the aims of the present paper, was made by Crowdy (2011). While Philip (1972) gave analytical solutions for both longitudinal and transverse shear flow over a periodic array of flat no-shear menisci in an otherwise no-slip surface, Crowdy (2011) generalised those solutions to flows over a wider class of periodic surfaces having more than one no-shear meniscus per period, with those menisci in each period window having general positioning. For the case of unbounded shear flow, the analysis for both longitudinal and transverse flow can be reduced to the search for an analytic function that Crowdy (2011) showed could be found by considering special classes of conformal slit mappings. Those slit mappings can, in turn, be expressed

in terms of transcendental functions called prime functions appropriate to the relevant pre-image domain (Crowdy 2011, 2020). This conformal slit mapping approach, differing from Philip's, which relied on Schwarz–Christoffel mapping theory, retrieves Philip's solutions as a special case. The parametric representation of the solutions as presented by Crowdy (2011) also has the mathematical advantage that square-root branch points associated with the transition points from no-slip to no-shear do not appear explicitly, making their numerical evaluation easier.

The aim of the present paper is similar to that of Crowdy (2011): to take another solution found by Philip (1972), namely, longitudinal pressure-driven flow along a superhydrophobic pipe, and generalise it to a more diverse class of no-shear surface patterning. Of interest here is Philip's analytical solution for an axial pressure-driven flow, having the form $\mathbf{u} = (0, 0, w_{philip})$ in a Cartesian $(x, y, Z)$ plane, through a superhydrophobic pipe with $N$ no-shear stripes on its boundary, which are restricted to be rotationally symmetric and of equal individual circumferential length $2\Phi$ (assuming a unit radius pipe). Such SHS pipes are of great practical importance for reducing drag in various fluidic systems. However, the manufacturing process is often stochastic, i.e. the finished surfaces are geometrically heterogeneous. By generalising the symmetric approach provided by Philip, an important step is taken towards the exploration of real SHS configurations. Philip found the axial velocity field solution as an explicit function of the complex variable $z = x + \mathrm{i}y$:

$$w_{philip} = \left( \frac{1 - |z|^2}{4} + \frac{1}{N} \operatorname{Im} \left[ \cos^{-1} \left( \frac{\cos(\kappa(z))}{\cos(\Phi/2)} \right) - \kappa(z) \right] \right) \tag{1.1}$$

and

$$\kappa(z) = -\frac{\mathrm{i}N}{2} \log z. \tag{1.2}$$

The complex variable $z$ is normalised with respect to the outer pipe radius $R_0$ and the velocity $w$ by $sR_0^2/\mu$, where $s$ is the negative pressure gradient, and $\mu$ is the dynamic fluid viscosity. The corresponding effective slip length $\lambda_{eff}^{(P)}$ based on Philip's model (Lauga & Stone 2003) is given by

$$\lambda_{eff}^{(P)} = \frac{2}{N} \log \left( \sec \left( \frac{N\Phi}{2} \right) \right). \tag{1.3}$$

In any cross-section of the pipe at a fixed value of $Z$, the no-shear stripes along the length of the pipe resemble a two-dimensional 'meniscus', so it is convenient to use that designation throughout.

In the present paper, this solution of Philip (1972) is generalised to allow for a much more diverse array of no-shear patterns around the circular pipe boundary, including cases with unequally sized menisci and no rotational symmetry at all. Remarkably, these generalised solutions can also be found in analytical form, a result of some theoretical significance. The results here are the radial geometry (or pipe flow) analogue of the generalisation of Philip's solutions for shear-driven flow over flat SHS presented in Crowdy (2011). Just as in that study, a key role is played by the prime function machinery (Crowdy *et al.* 2016; Crowdy 2020). Moreover, the solutions are given in a parametric form that shares the benefit of the shear-flow solutions of Crowdy (2011) in encoding the square-root branch points at the no-slip/no-shear transition points in an implicit way that obviates the need for careful branch-cut choices in the numerical evaluation of the solutions.

Philip (1972) himself made extensive use of conformal mapping in solving many of the problems in his paper; this is a natural choice for certain of the problems considered

by him, for example, for simple longitudinal shear over a periodic array of flat no-shear 'slots' in an otherwise no-slip surface, a problem generalised by Crowdy (2011). The boundary value problem in that case involves Laplace's equation and enjoys the property of conformal invariance. However, a complication associated with the pressure-driven pipe flow considered by Philip (1972) – the generalisation of which is the topic of the present paper – is that it is governed by a special form of Poisson's equation – that is, Laplace's equation with a non-zero constant forcing function – and, as a result, is not conformally invariant. Nevertheless, as will be shown here, a wide class of generalised solutions to this boundary value problem for Poisson's equation can be found. These solutions are important not just because they solve the problems considered here; remarkably, the same boundary value problems recur in a large number of physical problems, rendering the new solutions here of broad significance in the physical sciences (Bazant 2016). This matter is discussed again later.

The outline of the paper is as follows. After a description of the relevant mixed boundary value problem given in § 2, the single meniscus problem solved by Philip (1972) is rederived in § 3 using a novel geometrical approach based on prime functions and conformal slit mappings akin to that used previously by Crowdy (2011) to derive some of Philip's other solutions for shear flow over periodic SHS. The effective slip length is defined in § 4, and a formula for it, also in terms of prime functions, is established. Sections 5 and 6 show how the mathematical approach expounded in § 3 generalises in a natural way to the case of two ($M = 2$) and three ($M = 3$) no-shear menisci, respectively. Illustrative calculations are included in both cases. Section 7 shows how a simple additional conformal map can be used to take the solution for any pattern of $M \geqslant 1$ no-shear menisci to produce a generalised solution for flow in another pipe where (a rescaled version of) that no-shear pattern appears in each $2\pi/N$ sector of an $N$-fold rotationally symmetric arrangement for any integer $N \geqslant 1$. Finally, § 8 features a summary and discussion of the results, including some remarks on the broader physical significance of the mathematical results.

## 2. A boundary value problem of mixed type

In a Cartesian $(x, y, Z)$ plane, let $\boldsymbol{u} = (0, 0, w(x, y))$ be the steady, fully developed, pressure-driven flow in the axial $Z$ direction of a fluid, specifically a liquid rather than a gas, of viscosity $\mu$, through a circular pipe of radius $R_0$ having a cross-section in the $(x, y)$ plane, denoted by $D_z$. The pipe is superhydrophobic and is assumed to have $M \geqslant 1$ no-shear menisci separated by solid wall portions; later, superhydrophobic pipes with an $N$-fold rotationally symmetric array of menisci with $M$ menisci per $2\pi/N$ sector will also be considered. It is assumed that all menisci match the curvature of the pipe wall. However, depending on external influences, there may be additional interface deflection, in which case the present interface shape should be understood as a first approximation; this matter is discussed again in § 8. For the analysis that follows, no potential influence of surfactant depositions at the interface is considered. The axial, or longitudinal, velocity $w(x, y)$ in such a pipe is governed by

$$\nabla^2 w = -\frac{s R_0^2}{\mu} = -1, \quad \nabla^2 = \frac{\partial}{\partial x^2} + \frac{\partial}{\partial y^2}, \tag{2.1}$$

where the flow is driven by a constant pressure gradient $s$ along the $Z$-axis in the domain $0 \leqslant |(x, y)| < 1$. Lengths are normalised with respect to the outer-wall radius $R_0$, and the velocity with respect to $sR_0^2/\mu$. At the pipe boundary, the Poisson problem (2.1) has a

mixture of two types of boundary conditions: either a no-slip condition on any portion of solid wall, or a no-shear condition on any meniscus. These can be expressed as

$$w = 0 \quad \text{on } |(x, y)| = 1 \quad \text{(no slip parts)}, \tag{2.2}$$

$$\frac{\partial w}{\partial n} = 0 \quad \text{on } |(x, y)| = 1 \quad \text{(no shear parts)}, \tag{2.3}$$

where $\partial/\partial n$ denotes the derivative in the normal direction, pointing into the viscous fluid, at the circular pipe boundary.

It is expedient to express this mixed boundary value problem in terms of the complex variable $z = x + \mathrm{i}y$. A flow governed by the linear partial differential equation (2.1) subject to (2.2) and (2.3) can be written as the sum of a particular solution $w_{ps}$ and a harmonic part $w_h$, i.e.

$$w = w_{ps} + w_h, \tag{2.4}$$

with

$$w_{ps} = \frac{1 - |z|^2}{4}, \quad w_h = \mathrm{Re}\,[h(z)]\,, \tag{2.5}$$

where non-dimensionalised Poiseuille flow is chosen as the particular solution $w_{ps}$, and $\mathrm{Re}[\cdot]$ denotes the real part of the quantity in square brackets. The harmonic part $w_h$, which is the real part of an analytic function $h(z)$, a complex potential, serves as a correction to the Poiseuille flow that takes into account the influence of the shear-free menisci on the velocity field. In this way, the problem is reduced to finding a complex potential $h(z)$, analytic in $D_z$, whose real part is the required $w_h$.

The challenge then is to determine $h(z)$. To do so, it is necessary to express the mixed-type boundary conditions (2.2) and (2.3) in terms of it. By the choice of $w_{ps}$, the no-slip condition (2.2) gives

$$\mathrm{Re}\,[h(z)] = 0 \quad \text{on } |z| = 1 \quad \text{(no slip parts)}. \tag{2.6}$$

The no-shear condition (2.3) on $|z| = 1$ can be written as

$$\boldsymbol{\nabla} w \cdot \boldsymbol{n} = \mathrm{Re}\left[2\frac{\partial w}{\partial z}(-z)\right] = 0, \tag{2.7}$$

where use has been made of the fact that if the complex analogues of two vectors $\mathbf{a} = (a_x, a_y)$ and $\mathbf{b} = (b_x, b_y)$ are $a = a_x + \mathrm{i}a_y$ and $b = b_x + \mathrm{i}b_y$, then the analogue of the dot product $\mathbf{a} \cdot \mathbf{b}$ is $\mathrm{Re}[\bar{a}b]$, where $\bar{a}$ is the complex conjugate of $a$. Note that the complex form of $\boldsymbol{\nabla} w$ is $2\,\partial w/\partial \bar{z}$, and the complex form of the normal vector, pointing into the pipe, is $-z$. On use of (2.4), condition (2.7) is equivalent to

$$\mathrm{Re}\left[zh'(z)\right] = \frac{1}{2} \quad \text{on } |z| = 1 \quad \text{(no shear parts)}. \tag{2.8}$$

An important observation is that by the chain rule, and using the parametrisation $z = \mathrm{e}^{\mathrm{i}\theta}$ for $|z| = 1$,

$$\frac{\partial}{\partial \theta} = \mathrm{i}z\,\frac{\partial}{\partial z}, \tag{2.9}$$

so that (2.8) can alternatively be written as

$$\mathrm{Re}\left[-\mathrm{i}\,\frac{\partial}{\partial \theta}h(z)\right] = \mathrm{Im}\left[\frac{\partial}{\partial \theta}h(z)\right] = \frac{1}{2} \quad \text{on } |z| = 1 \quad \text{(no shear parts)}. \tag{2.10}$$

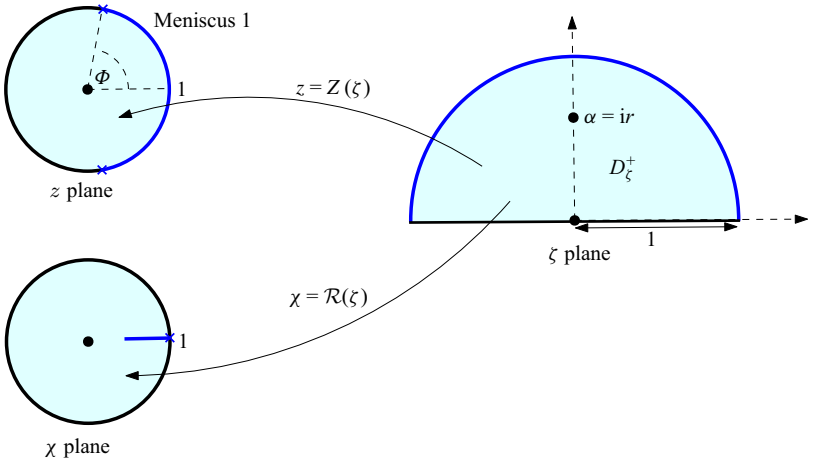


Figure 1. Conformal slit mappings $Z(\zeta)$ and $\mathcal{R}(\zeta)$ from an upper half unit disc $\{D_\zeta^+ : |\zeta| < 1,\ \mathrm{Im}[\zeta] \geqslant 0\}$ to a bounded circular slit domain (in a complex $z$ plane) and a bounded radial slit domain (in a complex $\chi$ plane). Corresponding images under the respective maps are colour-coded. The point $\zeta = \alpha$ is the pre-image of the origin in both cases.

This can be integrated with respect to $\theta$ on the $j$th no-shear portion to give

$$\mathrm{Im}[h(z)] = \frac{\theta}{2} + c_j, \tag{2.11}$$

where $c_j$ is a constant of integration. Without loss of generality, one of these constants can be set equal to zero.

In summary, the mathematical problem in the case of $M$ no-shear menisci is to find a function $h(z)$ analytic in $|z| < 1$ satisfying the mixed boundary conditions

$$\begin{cases} \mathrm{Re}[h(z)] = 0 & \text{on solid portions of } |z| = 1, \\ \mathrm{Im}[h(z)] = \theta/2 + c_j & \text{on meniscus } j \text{ of } |z| = 1, \end{cases} \tag{2.12}$$

where $z = \mathrm{e}^{\mathrm{i}\theta}$ for some set of real constants $\{c_j : j = 1, \ldots, M\}$.

## 3. A new derivation of the Philip (1972) single slot solution

It is useful to first retrieve Philip's solution (1.1)–(1.2) with $M = 1$ in a novel manner that differs from the original derivation in Philip (1972). It is then shown in §§ 5 and 6 how the analysis of this section generalises, in a straightforward way, to the more general case of $M > 1$ no-shear slots in general position on the pipe wall; this generalisation makes use of the prime function and conformal slit mapping machinery developed in Crowdy *et al.* (2016) and Crowdy (2020).

The problem to be solved is the situation where the pipe wall has a single shear-free meniscus occupying the sector

$$-\Phi < \arg[z] < \Phi \tag{3.1}$$

for some $\Phi \in [0, \pi)$. The first step is to introduce a conformal mapping from the upper half unit $\zeta$ disc, denoted by $D_\zeta^+ = \{\zeta : |\zeta| < 1,\ \mathrm{Im}[\zeta] > 0\}$ to the fluid inside the circular pipe; figure 1 shows a schematic. It is given by

$$z = Z(\zeta) \equiv -\frac{\omega(\zeta,\alpha)\,\omega(\zeta,1/\alpha)}{\omega(\zeta,\overline{\alpha})\,\omega(\zeta,1/\overline{\alpha})}, \quad \omega(\zeta,\alpha) = \zeta - \alpha, \quad \alpha = \mathrm{i}r, \tag{3.2}$$

for some $0 \leqslant r < 1$. Using this definition, it is easy to check that the upper half unit semicircle, denoted by $C_0^+$, is transplanted to a portion of the circle $|z| = 1$, while the real diameter $-1 < \zeta < 1$ is transplanted to the remainder of this circle. It is also easily verified that

$$Z(0) = -1, \quad Z(1) = \left(\frac{1-\alpha}{1+\alpha}\right)^2, \quad Z(\mathrm{i}) = 1. \tag{3.3}$$

The semicircle $C_0^+$ can be identified with the pre-image of the meniscus, and the real diameter $-1 < \zeta < 1$ is the pre-image of the no-slip portion of the pipe wall. The centre of the meniscus at $z = 1$ is $\zeta = \mathrm{i}$. The pre-image of the edge of the meniscus in the lower half-plane, i.e. at $z = \mathrm{e}^{-\mathrm{i}\Phi}$, is $\zeta = 1$, meaning that

$$Z(1) = \left(\frac{1-\alpha}{1+\alpha}\right)^2 = \left(\frac{1-\mathrm{i}r}{1+\mathrm{i}r}\right)^2 = \mathrm{e}^{-\mathrm{i}\Phi}, \quad \text{or} \quad \frac{1-\mathrm{i}r}{1+\mathrm{i}r} = \mathrm{e}^{-\mathrm{i}\Phi/2}. \tag{3.4}$$

Simple manipulation of this relation and use of familiar trigonometric identities yields

$$r = \tan(\Phi/4). \tag{3.5}$$

The simple monomial $\omega(\zeta,\alpha) = \zeta - \alpha$ can be identified as the prime function for the unit disc, while the form of the mapping (3.2) is an example of a bounded circular slit mapping. These concepts and their generalisations are discussed in detail by Crowdy (2020).

It is useful now to write down another conformal slit mapping to a complex $\chi$ plane, called a radial slit mapping (Crowdy 2020), having a form very similar to (3.2) but defined by

$$\chi = \mathcal{R}(\zeta) \equiv -\frac{\omega(\zeta,\alpha)\,\omega(\zeta,1/\overline{\alpha})}{\omega(\zeta,\overline{\alpha})\,\omega(\zeta,1/\alpha)}. \tag{3.6}$$

Notice that while the first terms in the numerators and denominators of (3.2) and (3.6) are the same, the second terms have been swapped. The image of $D_\zeta^+$ under this mapping is the interior of the circular disc $|\chi| < 1$, with $C_0^+$ being transplanted to a radial slit on the positive real $\chi$-axis, and the real diameter $-1 < \zeta < 1$ being transplanted to the entire circle $|\chi| = 1$. It is easy to check, using (3.6), that

$$\mathcal{R}(1) = 1, \quad \mathcal{R}(-1) = 1. \tag{3.7}$$

Given explicit knowledge of the conformal mapping $Z(\zeta)$, the composed function

$$H(\zeta) \equiv h(Z(\zeta)) \tag{3.8}$$

can be introduced, which, by virtue of the respective analyticity properties of $h(z)$ and $Z(\zeta)$, is analytic in $D_\zeta^+$. In view of (2.12), on the boundary of $D_\zeta^+$ it must satisfy

$$\begin{cases} \mathrm{Re}[H(\zeta)] = 0 & \text{on } -1 < \zeta < 1, \\ \mathrm{Im}[H(\zeta)] = \theta/2 & \text{on } C_0^+, \end{cases} \tag{3.9}$$

where $z = Z(\zeta) = \mathrm{e}^{\mathrm{i}\theta}$, and where the single constant of integration in this $M = 1$ problem has been set to zero. This can also be written as

$$\begin{cases} \mathrm{Re}[H(\zeta)] = 0 & \text{on } -1 < \zeta < 1, \\ \mathrm{Im}[H(\zeta)] = -\dfrac{\mathrm{i}\log Z(\zeta)}{2} & \text{on } C_0^+. \end{cases} \tag{3.10}$$

It will now be argued that the expression

$$H(\zeta) = \frac{1}{2}\left(\log Z(\zeta) - \log \mathcal{R}(\zeta)\right), \tag{3.11}$$

involving both the bounded circular slit mapping $Z(\zeta)$ and the radial slit mapping $\mathcal{R}(\zeta)$, is the required solution for $H(\zeta)$. Both mappings $Z(\zeta)$ and $\mathcal{R}(\zeta)$ have simple zeros at $\zeta = \alpha$ in $D_\zeta^+$, but the resulting logarithmic singularities cancel out in (3.11), meaning that the function $H(\zeta)$ in (3.11) is analytic in $D_\zeta^+$, as required. Since the real diameter $-1 < \zeta < 1$ is transplanted to a unit circle (in the respective target plane) by both slit mappings $Z(\zeta)$ and $\mathcal{R}(\zeta)$, it is easy to check that $\mathrm{Re}[H(\zeta)] = 0$ on this real diameter; thus (3.11) satisfies the first of the boundary conditions in (3.10). And since $C_0^+$ is transplanted by $\mathcal{R}(\zeta)$ to a radial slit on the positive real $\chi$-axis, so that $\arg[\mathcal{R}(\zeta)] = 0$ for $\zeta \in C_0^+$, it is just as easy to verify that (3.11) also satisfies the second of the boundary conditions in (3.10).

Expression (3.11) is a convenient parametric form of Philip's single slot solution (Philip 1972). It is shown in Appendix A how to retrieve (1.1)–(1.2) for $N = 1$ from (3.11). A significant advantage of the parametric form (3.11) is that the square-root branch points in $h(z)$ at the edge of the no-shear slots do not appear explicitly, and are accounted for implicitly by use of the parametric variable $\zeta$.

## 4. Effective slip length

It is now possible to calculate the so-called effective slip length $\lambda_{eff}$ representing the averaged influence of the no-shear boundary segments on the axial velocity field, providing a tool to quantify the degree to which given SHS diverge from being a no-slip wall. It involves equating the total volume flux $Q$ caused by a given pressure gradient $s$ to that of a suitable comparison flow $(0, 0, w_{ns}(x, y))$ driven by the same pressure gradient, containing a purely no-slip wall at $|z| = 1$. The effective slip length is the value of $\lambda_{eff}$ for which

$$Q_{ns} = Q(\lambda_{eff}). \tag{4.1}$$

To evaluate this quantity, consider first a general axisymmetric pipe flow solution of

$$\boldsymbol{\nabla}^2 w^* = -1 \tag{4.2}$$

subject to

$$w^* = \lambda_{eff}\,\frac{\partial w^*}{\partial n}. \tag{4.3}$$

This problem has the solution

$$w^* = \frac{1 - |z|^2}{4} + \frac{\lambda_{eff}}{2}, \tag{4.4}$$

describing an axisymmetric pressure-driven pipe flow with constant slip $\lambda_{eff}$ at the outer wall, which can be interpreted as the effective slip length. By integrating (4.4) over the pipe cross-section, the associated volume flux is found to be

$$Q = \frac{\pi}{8} + \frac{\pi}{2}\lambda_{eff}. \tag{4.5}$$

An explicit expression for the effective slip length is then found by rearranging the ratio $Q/Q_{ns}$ such that

$$\lambda_{eff} = \frac{1}{4}\left(\frac{Q}{Q_{ns}} - 1\right), \tag{4.6}$$

where $Q_{ns}$ denotes the reference no-slip flow value. It is natural to take the comparison flow to be Poiseuille flow through the pipe for which $Q_{ns} = \pi/8$.

It remains to find the mass flux $Q$ associated with the solution of the mixed boundary value problems solved earlier. In view of the decomposition (2.4), it is natural to write

$$Q = Q_{ns} + Q_h, \tag{4.7}$$

where

$$Q_h = \iint_{D_z} w_h \, \mathrm{d}A = \iint_{D_z} \mathrm{Re}\,[h(z)] \, \mathrm{d}A \tag{4.8}$$

so that the effective slip length is given by

$$\lambda_{eff} = \frac{1}{4}\left(\frac{Q_{ns} + Q_h}{Q_{ns}} - 1\right) = \frac{1}{4}\frac{Q_h}{Q_{ns}} = \frac{2}{\pi} Q_h. \tag{4.9}$$

Let $\partial D_z$ denote the pipe boundary. The complex form of the Stokes theorem implies

$$Q_h = \mathrm{Re}\left[\int_{D_z} h(z)\, \mathrm{d}A\right] = \mathrm{Re}\left[\frac{1}{2\mathrm{i}} \oint_{\partial D_z} h(z)\, \bar{z}\, \mathrm{d}z\right] = \mathrm{Re}\left[\frac{1}{2\mathrm{i}} \oint_{\partial D_z} h(z)\, \frac{\mathrm{d}z}{z}\right], \tag{4.10}$$

where the fact that $\bar{z} = 1/z$ on $\partial D_z$ has been used. But $h(z)$ is analytic in $D_z$, so by the residue theorem,

$$Q_h = \mathrm{Re}\left[2\pi\mathrm{i} \times \frac{h(0)}{2\mathrm{i}}\right] = \pi\, \mathrm{Re}[h(0)]. \tag{4.11}$$

It follows that

$$Q_h = \pi \log\left|\frac{\omega(\alpha,\, 1/\alpha)}{\omega(\alpha,\, 1/\overline{\alpha})}\right|, \tag{4.12}$$

where (3.11), (3.2) and (3.6) have been used. It follows from (4.9) and (4.12) that

$$\lambda_{eff} = \frac{2}{\pi} Q_h = 2 \log\left|\frac{\omega(\alpha,\, 1/\alpha)}{\omega(\alpha,\, 1/\overline{\alpha})}\right|. \tag{4.13}$$

This expression for the effective slip length in terms of the prime function of the pre-image domain, in this case the unit $\zeta$ disc, is an important new result of this paper. Exactly the same formula will be found in the following sections to give the effective slip length for a wide range of superhydrophobic pipes with more general no-shear patterns, the only modification being that the appropriate prime function $\omega(\cdot, \cdot)$ relevant to each pipe must be used in (4.13).

On use of the definition (3.2) of the prime function for the unit disc, it follows from (4.13) that

$$\lambda_{eff} = 2 \log\left|\frac{\alpha - 1/\alpha}{\alpha - 1/\overline{\alpha}}\right| = 2 \log\left|\frac{1 + r^2}{1 - r^2}\right| = 2 \log\left(\sec\left(\frac{\Phi}{2}\right)\right), \tag{4.14}$$

where (3.5) and some trigonometric double-angle formulae have been used. In this way, Philip's slip length result (1.3) for a single slot is retrieved. As will be seen shortly, other choices of prime function used in (4.13) will give different results.

## 5. Exact solution for $M = 2$ unequal menisci

Consider a superhydrophobic pipe, with cross-section again denoted by $D_z$, now having $M = 2$ generally unequal menisci separated by solid portions with total solid fraction equal

to $\phi$, and each having equal circumferential length. The latter restriction is not necessary, and is easily lifted, but it makes presentation of the results clearer. According to the analysis in § 2, the problem reduces to finding a function $h(z)$, analytic inside $D_z$ and satisfying the mixed boundary conditions

$$\begin{cases} \mathrm{Re}[h(z)] = 0 & \text{on solid portions of } |z| = 1, \\ \mathrm{Im}[h(z)] = \theta/2 & \text{on meniscus 1 of } |z| = 1, \\ \mathrm{Im}[h(z)] = \theta/2 + c_2 & \text{on meniscus 2 of } |z| = 1, \end{cases} \tag{5.1}$$

for some real constant $c_2$.

In view of the new derivation of Philip's single meniscus solution in § 3, and motivated by the use of conformal slit mappings in solving mixed boundary value problems of this kind as originally proposed by Crowdy (2011), it is now posed that a parametric solution for $h(z)$ satisfying the boundary conditions (2.12) is given by

$$z = Z(\zeta), \quad h = H(\zeta) = \tfrac{1}{2}\left(\log Z(\zeta) - \log \mathcal{R}(\zeta)\right), \tag{5.2}$$

where the parametric complex variable $\zeta$ takes values in the upper half-annulus $\{D_\zeta^+ : \rho < |\zeta| < 1,\ \mathrm{Im}[\zeta] \geqslant 0\}$, and

$$Z(\zeta) \equiv -\frac{\omega(\zeta, \alpha)\,\omega(\zeta, 1/\alpha)}{\omega(\zeta, \overline{\alpha})\,\omega(\zeta, 1/\overline{\alpha})}, \quad \mathcal{R}(\zeta) \equiv -\frac{\omega(\zeta, \alpha)\,\omega(\zeta, 1/\overline{\alpha})}{\omega(\zeta, \overline{\alpha})\,\omega(\zeta, 1/\alpha)}, \tag{5.3}$$

for

$$\omega(\zeta, \alpha) = -\frac{\alpha}{C^2}\,P(\zeta/\alpha, \rho), \quad C = \prod_{n=1}^{\infty}\left(1 - \rho^{2n}\right), \tag{5.4}$$

with $\alpha = \mathrm{i}r$ for $\rho < r < 1$, and where

$$P(\zeta, \rho) = (1 - \zeta)\,\hat{P}(\zeta, \rho), \quad \hat{P}(\zeta, \rho) \equiv \prod_{n=1}^{\infty}\left(1 - \rho^{2n}\zeta\right)\left(1 - \rho^{2n}/\zeta\right). \tag{5.5}$$

In (5.2), the principal branch of the complex logarithm is assumed with $\log X = \log|X| + \mathrm{i}\arg[X]$, where $-\pi < \arg[X] \leqslant \pi$ so that the logarithm of a negative real quantity has imaginary part $\mathrm{i}\pi$.

Functionally, these formulae look identical to those in § 3, but there is a small but significant difference: the function $\omega(\zeta, \alpha)$ is no longer defined by $\omega(\zeta, \alpha) = \zeta - \alpha$, which is the prime function associated with the unit $\zeta$ disc. Instead, $\omega(\zeta, \alpha)$ now denotes the prime function for the concentric annulus $\{D_\zeta : \rho < |\zeta| < 1\}$ (see chapters 5 and 14 of Crowdy 2020), although its dependence on the parameter $\rho$ is suppressed in the notation. An important feature is that the prime function $\omega(\zeta, \alpha)$ has a simple zero when $\zeta = \alpha$. On substitution of (5.4) into (5.3), it is also possible to write

$$Z(\zeta) \equiv -\frac{P(\zeta/\alpha, \rho)\,P(\zeta\alpha, \rho)}{P(\zeta/\overline{\alpha}, \rho)\,P(\zeta\overline{\alpha}, \rho)}, \quad \mathcal{R}(\zeta) \equiv -\frac{P(\zeta/\alpha, \rho)\,P(\zeta\overline{\alpha}, \rho)}{P(\zeta/\overline{\alpha}, \rho)\,P(\zeta\alpha, \rho)}, \tag{5.6}$$

which highlights the dependence of $Z(\zeta)$ and $\mathcal{R}(\zeta)$ on $\rho$. The formulae (5.6) will be used in what follows. It is a straightforward exercise to show, directly from the infinite product representation (5.5), that $P(\zeta, \rho)$ satisfies the two functional relations

$$P(1/\zeta, \rho) = -\zeta^{-1}\,P(\zeta, \rho), \quad P(\rho^2\zeta, \rho) = -\zeta^{-1}\,P(\zeta, \rho). \tag{5.7}$$

The two functions (5.6) built using the prime function are, respectively, further examples of a circular slit map and a radial slit map as described in Crowdy & Marshall (2006)

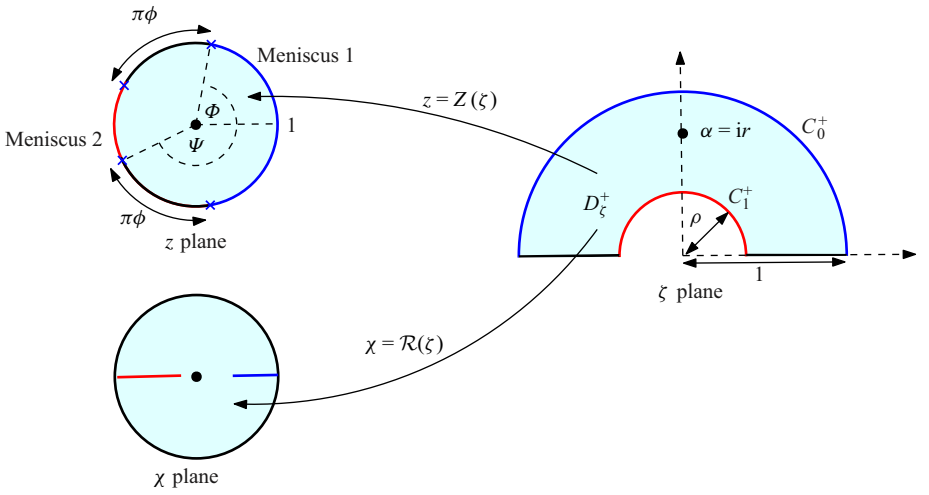


Figure 2. Conformal slit mappings $Z(\zeta)$ and $\mathcal{R}(\zeta)$ from an upper half-annulus $\{D_\zeta^+ : \rho < |\zeta| < 1,\ \mathrm{Im}[\zeta] \geqslant 0\}$ to a bounded circular slit domain (in a complex $z$ plane) and a bounded radial slit domain (in a complex $\chi$ plane). Corresponding images under the respective maps are colour-coded. The point $\zeta = \alpha$ is the pre-image of the origin in both the $z$ and $\chi$ planes.

and Crowdy (2011, 2020). The difference compared with those already presented in § 3 is that there are now $M = 2$ pre-image circles $C_0^+$ and $C_1^+$, and consequently, two circular arc slit images and two radial slit images; in § 3, $C_1^+$ was clearly absent. The properties (5.7) can be used to confirm that the colour-coded images of the boundary portions of the upper half-annulus $D_\zeta^+$ under these two mappings are as shown in figure 2. In particular, the upper half unit circle, denoted by $C_0^+$, is taken to be the pre-image of the blue meniscus centred at $z = 1$, and the upper half-circle $|\zeta| = \rho$, denoted by $C_1^+$, is the pre-image of the red meniscus centred at $z = -1$. The two intervals on the real axis, $-1 < \zeta < -\rho$ and $\rho < \zeta < 1$, are taken to be the pre-images of the two no-slip boundary portions of the pipe. From these geometrical properties, it can be verified, using properties of the complex logarithm, that $h(z)$ as given in (5.2) satisfies all the boundary conditions (2.12).

The mapping function $Z(\zeta)$ satisfies the functional identity

$$Z(-\overline{\zeta}) = -\frac{P(-\overline{\zeta}/\alpha,\, \rho)\; P(-\overline{\zeta}\alpha,\, \rho)}{P(-\overline{\zeta}/\overline{\alpha},\, \rho)\; P(-\overline{\zeta}\overline{\alpha},\, \rho)} = -\frac{P(\overline{\zeta}/\overline{\alpha},\, \rho)\; P(\overline{\zeta}\overline{\alpha},\, \rho)}{P(\overline{\zeta}/\alpha,\, \rho)\; P(\overline{\zeta}\alpha,\, \rho)} = \overline{Z(\zeta)}, \tag{5.8}$$

which reveals that the image of any point $\zeta$ and that of $-\overline{\zeta}$ (the reflection of $\zeta$ in the imaginary $\zeta$-axis) are complex conjugates of each other in the $z$ plane. This symmetry has two consequences. First, since $C_0^+$ and $C_1^+$ are taken to be the pre-images of the two menisci, the pre-images of their centres are at $\zeta = \mathrm{i}, \mathrm{i}\rho$. Indeed, it can be verified that

$$Z(\mathrm{i}) = 1, \quad Z(\mathrm{i}\rho) = -1, \tag{5.9}$$

and the two menisci are reflectionally symmetric about the $x$-axis. The symmetry (5.8) also confirms that the lengths of the images of the two segments of the real axis $-1 < \zeta < -\rho$ and $\rho < \zeta < 1$, which are taken to be the pre-images of the two solid portions, must have the same circumferential lengths since the image of one is the reflection about the $x$-axis of the other.

It is useful to remark here that to generalise the analysis to no-slip boundary portions of different lengths, it is simply necessary to allow the parameter $\alpha$ to move off the imaginary $\zeta$-axis but to remain in the upper half-annulus.

The conformal mapping in (5.6) depends on two unknown real parameters: $r$ and $\rho$. For given values of the angles $\Phi$ and $\Psi$ indicated in figure 2, the values of these two parameters are found by solving the equations

$$Z(-1) = \mathrm{e}^{\mathrm{i}\Phi}, \quad Z(-\rho) = \mathrm{e}^{\mathrm{i}\Psi}, \quad \Psi = \Phi + \pi\phi, \tag{5.10}$$

where $\phi$ is the solid fraction, so that $\pi\phi$ is the circumferential length of one of the solid portions. This is readily done using a nonlinear solver such as Newton's method.

Concerning the radial slit mapping, the two functional relations (5.7) can be used to show that the images of both $C_0^+$ and $C_1^+$ have constant argument. Indeed, it can be verified using (5.6) that

$$\mathcal{R}(\mathrm{i}) = \left(\frac{P(+r,\,\rho)}{P(-r,\,\rho)}\right)^2, \quad \mathcal{R}(\mathrm{i}\rho) = -\left(\frac{P(\rho r,\,\rho)}{P(-\rho r,\,\rho)}\right)^2, \tag{5.11}$$

revealing that the images under the radial slit mapping, in a complex $\chi$ plane say, of the points $\zeta = \mathrm{i}, \mathrm{i}\rho$ (corresponding to the centres of menisci 1 and 2), are, respectively, on the positive and negative real $\chi$-axis; indeed, these correspond to the ends, inside the unit $\chi$ disc, of the blue and red radial slits shown in figure 2.

With these geometrical properties of the two conformal slit mappings $Z(\zeta)$ and $\mathcal{R}(\zeta)$ established, it is easy to verify, using the properties of the principal branch of the complex logarithm, that they satisfy

$$\begin{cases} \mathrm{Im}[\log Z(\zeta)] = \theta & \text{on meniscus 1,} \\ \mathrm{Re}[\log Z(\zeta)] = 0 & \text{on solid portions,} \\ \mathrm{Im}[\log Z(\zeta)] = \theta & \text{on meniscus 2,} \end{cases} \tag{5.12}$$

and

$$\begin{cases} \mathrm{Im}[-\log \mathcal{R}(\zeta)] = 0 & \text{on meniscus 1,} \\ \mathrm{Re}[-\log \mathcal{R}(\zeta)] = 0 & \text{on solid portions,} \\ \mathrm{Im}[-\log \mathcal{R}(\zeta)] = -\pi & \text{on meniscus 2.} \end{cases} \tag{5.13}$$

From these observations, the form of the required solution (5.2) satisfying (5.1) is now clear. Arguments the same as in § 4 lead to the deduction that formula (4.13) continues to give the relevant effective slip length, but now with $\omega$ representing the appropriate prime function. In this case, it can be rewritten as

$$\lambda_{eff} = 2\log\left|\frac{P(-r^2,\,\rho)}{P(+r^2,\,\rho)}\right|. \tag{5.14}$$

It is worth mentioning that this closely resembles a slip length formula for shear flow over SHS with periodic arrays of no-shear slots as found by Crowdy (2011).

The problem of a single meniscus, the case $M = 1$, corresponds to the $\rho \to 0$ limit of the above analysis. The pre-image $\zeta$ annulus reduces in this limit to the unit $\zeta$ disc. And from (5.4), as $\rho \to 0$, the prime function for the concentric annulus $\rho < |\zeta| < 1$ reduces to the prime function for the unit disc (Crowdy 2020), namely,

$$\omega(\zeta,\,\alpha) = \zeta - \alpha, \tag{5.15}$$

while $P(\zeta,\,\rho) \to (1-\zeta)$ so that (5.14) retrieves (4.14).

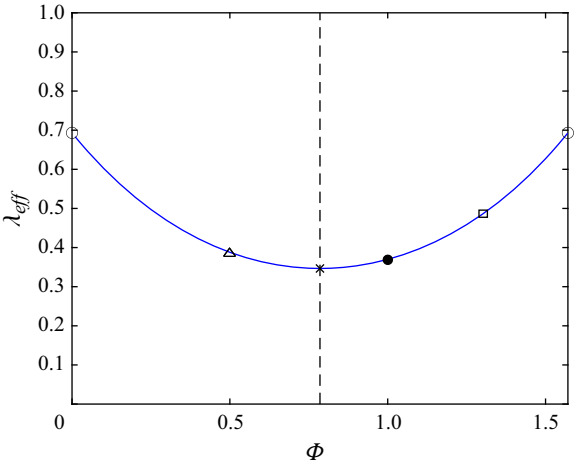


Figure 3. Graph of $\lambda_{eff}$ as a function of $\Phi$ for $M = 2$ no-shear menisci and two equal no-slip zones with solid fraction $\phi = 1/2$. The two open circles, at $\Phi = 0, \pi/2$, show Philip's result (1.3) for $N = 1$ and $\phi = 1/2$ since the configuration reduces to Philip's single meniscus solution retrieved in § 3. The cross, at $\Phi = \pi/4$, shows Philip's result (1.3) for $N = 2$ and $\phi = 1/2$ since the no-shear pattern has two fold rotational symmetry in this case. The new solutions interpolate between these known special cases. The triangle, filled circle and open square correspond to the contour plots in figure 4.

### 5.1. *Illustrative calculations*

Suppose that the solid fraction is chosen to be $\phi = 1/2$ so that the circumferential length of each solid portion is $2\pi\phi/2 = \pi/2$; figure 3 shows graphs of $\lambda_{eff}$, calculated using (5.14) as a function of $\Phi$. Thus $\Phi$ is in the range $0 \leqslant \Phi \leqslant \pi/2$: as $\Phi \to 0$, meniscus 1 (shown in blue in figure 2) disappears, while as $\Phi \to \pi/2$, meniscus 2 (shown in red in figure 2) disappears. These graphs are computed by first solving (5.10) for $r$ and $\rho$ given a value of $\Phi$ (and $\phi = 1/2$), and using these values to find $\lambda_{eff}$ from (5.14).

Several checks are available in this case. When $\Phi = 0, \pi/2$, the two no-slip zones merge, and one of the menisci disappears, leaving a pipe with a single meniscus and no-slip fraction equal to $\phi = 1/2$. The results of (5.14) should therefore coincide with (1.3) for $N = 1$ and $\phi = 1/2$, as corroborated by open circles in figure 3. When $\Phi = \pi/4$, the two no-slip zones have the same size as the two menisci, and the patterning on the pipe has symmetries about both the $x$- and $y$-axes (and a four fold rotational symmetry). The value of the effective slip length should then coincide with that given by (1.3) when $N = 2$ and $\phi = 1/2$, as corroborated by a cross in figure 3. The new analytical solution (5.2), for two non-equal menisci generally devoid of any rotational symmetry, can therefore be viewed as providing a continuous interpolating set between the rotationally symmetric $N = 1$ and $N = 2$ solutions, both with solid fraction $\phi = 1/2$.

Figure 4 shows contour lines of constant axial velocity for three different geometric configurations of superhydrophobic pipes, with $M = 2$ unequal shear-free menisci, for $\Phi = 0.5, 1, 1.3$. The slip lengths associated with these SHS pipes are indicated in figure 3 by a triangle, a filled circle and an open square, respectively.

## 6. Superhydrophobic pipe with $M > 2$ menisci

In the $M = 2$ analysis in § 5, the central role played by the prime function defined in (5.4), and associated with the concentric annulus relevant to that example, is apparent. The concentric annulus is an example of a doubly connected circular domain, a domain

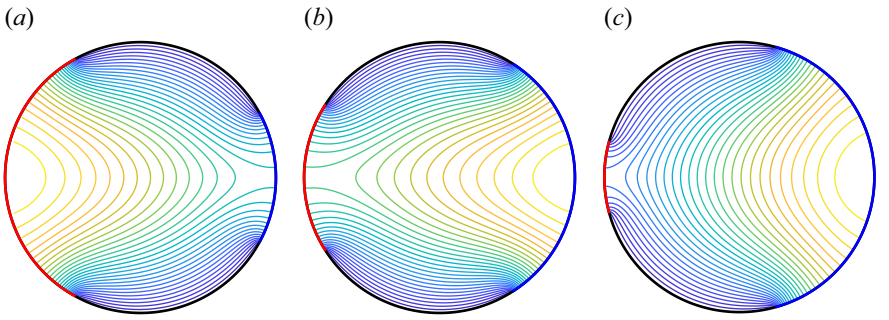


Figure 4. Constant axial velocity contours for superhydrophobic pipes with $M = 2$ unequal shear-free menisci, assuming $\phi = 1/2$: (*a*) $\Phi = 1/2$, (*b*) $\Phi = 1$, (*c*) $\Phi = 1.3$. The parameters $r$, $\rho$ are found by solving (5.10).

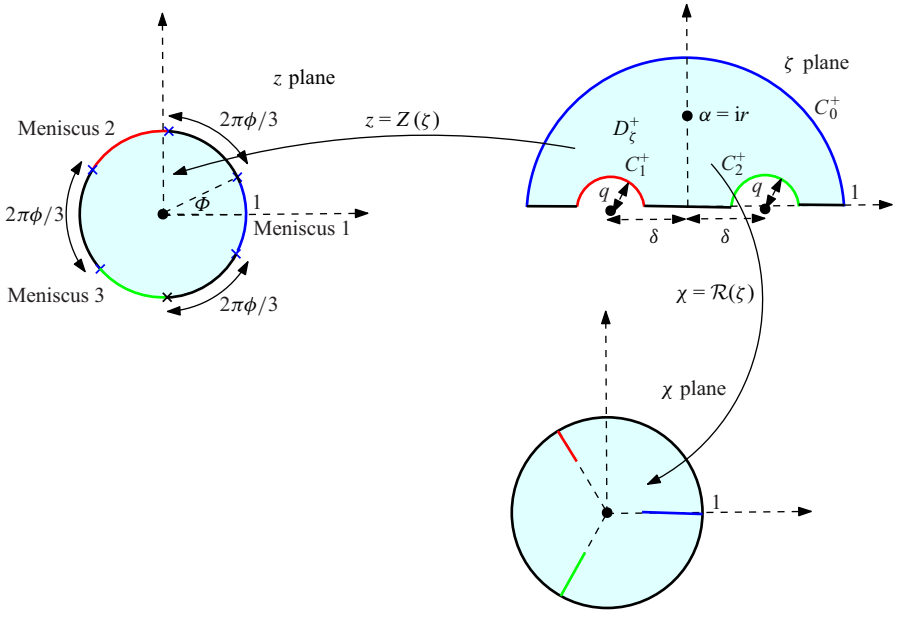


Figure 5. Conformal slit mappings $Z(\zeta)$ and $\mathcal{R}(\zeta)$ as given by (6.3) to a bounded circular slit domain (in a complex $z$ plane) and a bounded radial slit domain (in a complex $\chi$ plane). The image in the $z$ plane is the interior of a circular superhydrophobic pipe with $M = 3$ menisci punctuated by three solid portions of equal circumferential length. Corresponding images under the respective maps are colour-coded. The point $\zeta = \alpha$ is the pre-image of the origin in both the $z$ and $\chi$ planes.

whose boundaries are a union of circles. Prime functions can naturally be associated with any multiply connected circular domain, a mathematical fact whose theory has been expounded in detail in a recent monograph (Crowdy 2020). Equipped with this mathematical machinery, the generalisation of the $M = 2$ solution to any value of $M > 2$ is straightforward, a circumstance underscoring the theoretical importance of prime functions in applied mathematics (Crowdy 2020).

Suppose now that a superhydrophobic pipe, with cross-section denoted again by $D_z$, has $M = 3$ menisci in general positions around the boundary, punctuated by $M$ no-slip zones. Figure 5 shows such a superhydrophobic pipe with total solid fraction equal to $\phi$, and each having equal circumferential length; again, the latter restriction is not necessary and can

be lifted. The solution construction for this $M = 3$ case will now be set out, after which generalisation to any $M \geqslant 1$ should be obvious.

According to the analysis in § 2, the problem reduces to finding a function $h(z)$, analytic inside $D_z$ and satisfying the mixed boundary conditions

$$\begin{cases} \mathrm{Re}[h(z)] = 0 & \text{on solid portions of } |z| = 1, \\ \mathrm{Im}[h(z)] = \theta/2 & \text{on meniscus 1 of } |z| = 1, \\ \mathrm{Im}[h(z)] = \theta/2 + c_2 & \text{on meniscus 2 of } |z| = 1, \\ \mathrm{Im}[h(z)] = \theta/2 + c_3 & \text{on meniscus 3 of } |z| = 1. \end{cases} \tag{6.1}$$

The parametric solution for $h(z)$ using generalised conformal slit mappings is immediate given the prime function framework (Crowdy 2020). It is

$$z = Z(\zeta), \quad h(z) = H(\zeta) = \tfrac{1}{2}\left(\log Z(\zeta) - \log \mathcal{R}(\zeta)\right), \tag{6.2}$$

where the parametric complex variable $\zeta$ takes values in the upper half circular domain $D_\zeta^+$ also shown in figure 5, and

$$Z(\zeta) \equiv -\frac{\omega(\zeta, \alpha)\,\omega(\zeta, 1/\alpha)}{\omega(\zeta, \overline{\alpha})\,\omega(\zeta, 1/\overline{\alpha})}, \quad \mathcal{R}(\zeta) \equiv -\frac{\omega(\zeta, \alpha)\,\omega(\zeta, 1/\overline{\alpha})}{\omega(\zeta, \overline{\alpha})\,\omega(\zeta, 1/\alpha)}, \tag{6.3}$$

with $\alpha = \mathrm{i}r$ for $0 < r < 1$. The formulae (6.2) and (6.3) are exactly the same as in §§ 3 and 5, with the only difference being that the function $\omega(\cdot, \cdot)$ must now be taken to be the prime function associated with a triply connected circular domain $D_\zeta$ comprising the unit disc $|\zeta| \leqslant 1$ with two circular discs $|\zeta + \delta| < q$ and $|\zeta - \delta| < q$ excised; the unit circle will be denoted by $C_0$, and the two smaller circular boundaries $|\zeta + \delta| = q$ and $|\zeta - \delta| = q$ by $C_1$ and $C_2$, respectively. The domain $D_\zeta^+$ shown in figure 5 is the upper half of this circular domain $D_\zeta$. The general theory of prime functions associated with circular domains such as $D_\zeta$ can be found in Crowdy (2020), and Appendix B surveys methods by which these special functions can be evaluated. An important feature of every prime function $\omega(\zeta, \alpha)$ is that it has a simple zero when $\zeta = \alpha$. It has other mathematical properties that ensure that (6.3) continues to provide the requisite conformal slit mappings with the geometrical effect shown in figure 5 (Crowdy 2020).

The upper half of the unit circle is denoted again by $C_0^+$, while the upper halves of the circles $|\zeta + \delta| = q$ and $|\zeta - \delta| = q$ will be denoted by $C_1^+$ and $C_2^+$, respectively. For the superhydrophobic pipe problem with three no-shear menisci, the images of the upper half semicircles $C_0^+$, $C_1^+$, $C_2^+$ under the mapping $Z(\zeta)$ are taken to be the three no-shear menisci in the $z$ plane, with the correspondences colour-coded in figure 5; the no-slip zones are the images of the three portions of the real $\zeta$-axis, shown in black in figure 5. The semicircles $C_1^+$ and $C_2^+$ are taken to have the same radius, with centres symmetrically disposed about the $\zeta$ origin, and $\alpha$ has been placed on the imaginary axis inside $D_\zeta^+$ because these are necessary (but not sufficient) conditions for the three solid portions to have the same circumferential length.

In (6.2), the principal branch of the complex logarithm is assumed, and it is easy to show that the constants $c_2$ and $c_3$ in (6.1) are related to the arguments of the radial slits shown schematically in figure 5. Formulae, in terms of the prime function, for these constants can be derived, but they are not important for determining the flow or the effective slip length, so they are omitted here.

The mapping $Z(\zeta)$ now depends on three real parameters, $q$, $\delta$ and $r$. Suppose that the solid fraction is chosen to be $\phi = 1/2$ so that the circumferential length of each no-slip

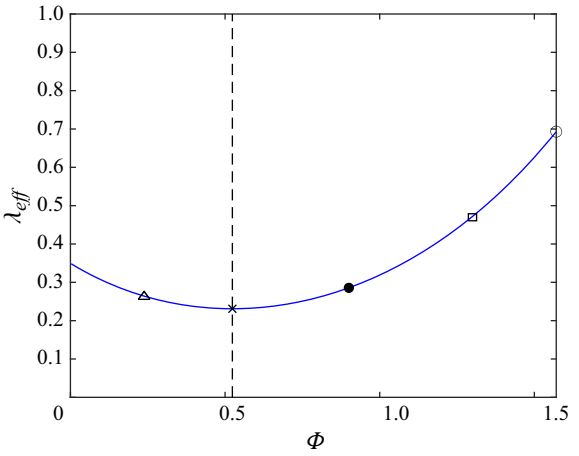


Figure 6. Graph of $\lambda_{eff}$ as a function of $\Phi$ for $M = 3$ no-shear menisci and three no-slip zones of fixed length $\pi/3$ so that the solid fraction is $\phi = 1/2$. The cross shows Philip's result (1.3) with $N = 3$ and $\phi = 1/2$ when $\Phi = \pi/6$, since at this value, the no-shear pattern has three fold rotational symmetry. The open circle shows the result (1.3) with $N = 1$ and $\phi = 1/2$ when $\Phi = \pi/2$, since at this value, the configuration corresponds to Philip's single meniscus case studied in § 3. The new solutions interpolate between these known special cases. The triangle, filled circle and open square correspond to the contour plots in figure 7.

region is $2\pi\phi/3 = \pi/3$. Then $q$, $\delta$ and $r$ must be chosen to satisfy the three conditions

$$Z(-1) = \mathrm{e}^{\mathrm{i}\Phi}, \quad Z(-\delta - q) = \mathrm{e}^{\mathrm{i}(\Phi+\pi/3)}, \quad Z(-\delta + q) = \mathrm{e}^{5\pi\,\mathrm{i}/6}, \tag{6.4}$$

where the angle $\Phi$ is shown in figure 5. A nonlinear solver such as Newton's method applied to (6.4) leads easily to the requisite values of $q$, $\delta q$, $\delta$ and $r$. It is important to emphasise that although the same function name $\omega(\cdot, \cdot)$ as in § 5 has been used, it now refers to a different function that can be readily calculated following the discussion in Appendix B. More details on how to compute the prime function can be found in Chapter 14 of Crowdy (2020).

The same arguments as used in § 4 lead to the deduction that (4.13) continues to give the relevant effective slip length, but now with $\omega$ representing the appropriate prime function.

### 6.1. *Illustrative calculations*

Figure 6 shows graphs of $\lambda_{eff}$ as functions of $\Phi$ for three no-slip zones with solid fraction $\phi = 1/2$ so that the circumferential length of each is $\pi/3$. This means that $\Phi$ takes values in the interval $0 \leqslant \Phi \leqslant \pi/2$: when $\Phi \to 0$, meniscus 1 (shown in blue in figure 5) disappears, while menisci 2 and 3 have the same circumferential length equal to $\pi/2$; when $\Phi = \pi/6$, all three menisci and the three solid portions have equal length $\pi/3$, and the pipe has three fold rotational symmetry; when $\Phi \to \pi/2$, menisci 2 and 3 have disappeared, and the problem reduces to the $M = 1$ solution with solid fraction $\phi = 1/2$. For each $\Phi$, the relevant values of $q$, $\delta$ and are found by solving (6.4) with those values, then used in (4.13) to compute the effective slip length. As a check on the calculation, the open circle in figure 6 shows the result (1.3) with and when; in this case, the superhydrophobic pipe has three fold rotational symmetry, and (1.3) applies.

Figure 7 illustrates the axial velocity contour lines for three distinct SHS pipes, each featuring $M = 3$ unequal shear-free menisci at $|z| = 1$, for $\Phi = 0.24, 0.9, 1.3$. The associated slip lengths for these SHS pipes are indicated in figure 6 by a triangle, a filled circle and an open square, respectively.

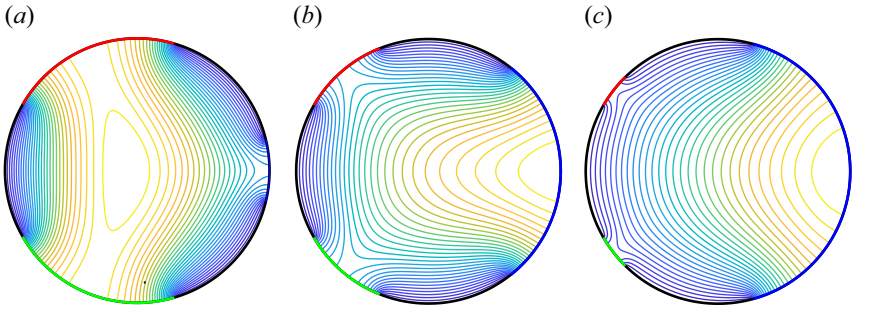


Figure 7. Axial velocity field contour lines for SHS pipes with $M = 3$ unequal shear-free menisci at $|z| = 1$ with $\phi = 1/2$: (*a*) $\Phi = 2.4$, (*b*) $\Phi = 0.9$, (*c*) $\Phi = 1.3$. The parameters $r, q, \delta$ are found by solving the three equations in (6.4).

## 7. The $N$-fold rotationally symmetric pipes with $M$ menisci per sector

Suppose now that there is an $N$-fold rotationally symmetric array of menisci with a single meniscus in each sector of opening angle $2\pi/N$. By the assumed rotational symmetry, it is enough to consider the problem in the sector

$$-\frac{\pi}{N} < \arg[z] < \frac{\pi}{N}, \tag{7.1}$$

where the meniscus is taken to occupy

$$-\Phi < \arg[z] < \Phi. \tag{7.2}$$

Under the conformal mapping

$$\mathcal{Z} = z^N, \tag{7.3}$$

this principal sector in the $z$ plane is transplanted to the entire unit disc in a complex $\mathcal{Z}$ plane with the meniscus now corresponding to the sector

$$-\tilde{\Phi} < \arg[z] < \tilde{\Phi}, \quad \tilde{\Phi} = N\Phi. \tag{7.4}$$

Figure 8 shows a schematic in the case $N = 4$ where there is just a single meniscus in the principal sector.

The original boundary value problem for $w(x, y)$ is a Poisson problem with mixed boundary conditions and is not therefore conformally invariant. However, the solution for the $N$-fold symmetric generalisation can still be written as (2.4), but with $h(z)$ now sought as a function of $\mathcal{Z}$, i.e.

$$h(z) = \mathcal{H}(\mathcal{Z}). \tag{7.5}$$

By the rotational symmetry of the original boundary value problem, $\mathcal{H}(\mathcal{Z})$ will be analytic and single-valued in $|\mathcal{Z}| \leqslant 1$. On the solid portions, it is still necessary that

$$\mathrm{Re}[\mathcal{H}(\mathcal{Z})] = 0. \tag{7.6}$$

However, on the no-shear portions, the boundary condition differs. This is because, by the chain rule,

$$z\frac{\partial}{\partial z} = N\mathcal{Z}\frac{\partial}{\partial \mathcal{Z}}, \tag{7.7}$$

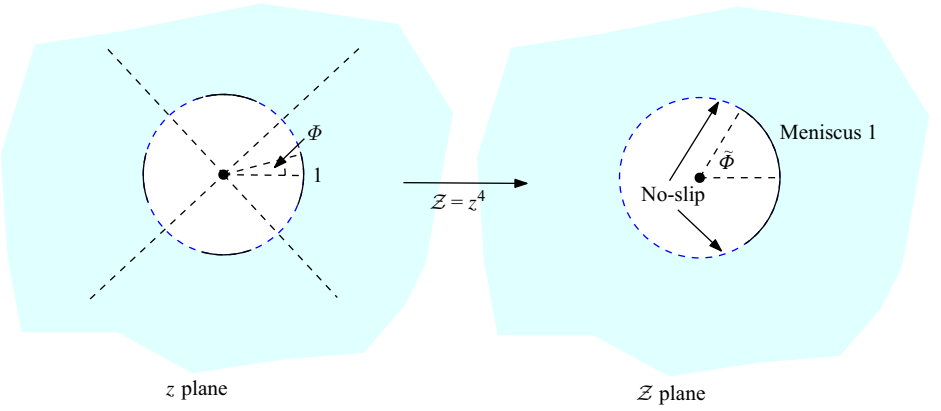


Figure 8. Conformal mapping (7.3) from a $2\pi/N$ sector in the $z$ plane to a full circle in a complex $\mathcal{Z}$ plane. The case $N = 4$ is shown with $M = 1$ meniscus per $2\pi/N$ sector.

so the no-shear condition (2.7) becomes

$$\mathrm{Re}\left[-\frac{z\bar{z}}{2} + N\mathcal{Z}\,\mathcal{H}'(\mathcal{Z})\right] = 0, \quad \text{or} \quad \mathrm{Re}\left[\mathcal{Z}\,\mathcal{H}'(\mathcal{Z})\right] = \frac{1}{2N}. \tag{7.8}$$

Letting $\mathcal{Z} = \mathrm{e}^{\mathrm{i}\Theta}$, the chain rule implies

$$\frac{\partial}{\partial\Theta} = \mathrm{i}\mathcal{Z}\,\frac{\partial}{\partial\mathcal{Z}}, \tag{7.9}$$

so that (7.8) can be written as

$$\mathrm{Im}\left[\frac{\partial}{\partial\Theta}\mathcal{H}(\mathcal{Z})\right] = \frac{1}{2N} \quad \text{on } |\mathcal{Z}| = 1 \quad \text{(no shear part)}. \tag{7.10}$$

This can be integrated with respect to $\Theta$:

$$\mathrm{Im}\left[\mathcal{H}(\mathcal{Z})\right] = \frac{\Theta}{2N} \quad \text{on } |\mathcal{Z}| = 1 \quad \text{(no shear part)}, \tag{7.11}$$

where a constant of integration has been set to zero without loss of generality.

This boundary value problem for $\mathcal{H}$ as a function of $\mathcal{Z}$ can be solved using the parametric $\zeta$ plane because it is now formally the same as the problem already solved in § 3. Indeed, a parametric representation of the solution is

$$\mathcal{Z} = Z(\zeta), \quad \mathcal{H} = \frac{1}{2N}\left(\log Z(\zeta) - \log \mathcal{R}(\zeta)\right), \tag{7.12}$$

where $Z(\zeta)$ and $\mathcal{R}(\zeta)$ are given by (3.2) and (3.6), but now with $\alpha = \mathrm{i}r$, where

$$r = \tan(\tilde{\Phi}/4). \tag{7.13}$$

The important point is that given any solution for $M \geqslant 1$ no-shear menisci such as those derived in § 3 for $M = 1$, in § 5 for $M = 2$, and for $M = 3$ in § 6, it can be composed with a mapping of the form (7.3) for any $N > 1$ to generalise that solution to the $N$-fold rotationally symmetric case. This means that the methodology of this paper provides a solution strategy for a wide class of superhydrophobic patternings.

The formula (4.13) for the effective slip length has to be modified by a simple multiplicative prefactor when $N > 1$. Let $\partial D_z$ denote the pipe boundary of an $N$-fold

rotationally symmetric pattern with $M$ menisci in each $2\pi/N$ sector. Let $\tilde{D}_z$ denote the principal sector (or pie slice), and let $\partial\tilde{D}_z$ denote the part of its boundary on $|z|=1$. The quantity $Q_{\mathrm{h}}$ is

$$Q_h = \mathrm{Re}\left[\int_{D_z} h(z)\,\mathrm{d}A\right] = N\,\mathrm{Re}\left[\int_{\tilde{D}_z} h(z)\,\mathrm{d}A\right], \tag{7.14}$$

where the $N$-fold symmetry has been used. By the complex form of Stokes' theorem,

$$Q_h = N\,\mathrm{Re}\left[\frac{1}{2\mathrm{i}}\int_{\partial\tilde{D}_z} h(z)\,\overline{z}\,\mathrm{d}z\right], \tag{7.15}$$

where the contributions from the two 'edges' of the sector can be shown to cancel out by the rotational symmetry. But now

$$Q_h = N\,\mathrm{Re}\left[\frac{1}{2\mathrm{i}}\int_{\partial\tilde{D}_z} h(z)\,\frac{\mathrm{d}z}{z}\right], \tag{7.16}$$

where the fact that $\overline{z}=1/z$ on $\partial\tilde{D}_z$ has been used. Now this contour integral can be transformed to the $\mathcal{Z}$ plane:

$$Q_h = N\,\mathrm{Re}\left[\frac{1}{2\mathrm{i}}\int_{\partial\tilde{D}_{\mathcal{Z}}} \mathcal{H}(\mathcal{Z})\,\frac{\mathrm{d}\mathcal{Z}}{N\mathcal{Z}}\right] = \mathrm{Re}\left[\frac{1}{2\mathrm{i}}\int_{\partial\tilde{D}_{\mathcal{Z}}} \mathcal{H}(\mathcal{Z})\,\frac{\mathrm{d}\mathcal{Z}}{\mathcal{Z}}\right], \tag{7.17}$$

where $\partial\tilde{D}_{\mathcal{Z}}$ denotes the image of $\partial\tilde{D}_z$ under the mapping (7.3). This equation is now identical to (4.10), the only difference being that the solution for $\mathcal{H}(\mathcal{Z})$ as a function of $\mathcal{Z}$ is now a factor of $1/N$ times the solution for $h(z)$ as a function of $z$; this is readily seen by comparing (7.12) with (3.11). It follows, on comparing (4.10) and (7.17) and making use of (4.9), that the slip length is also multiplied by a factor of $1/N$, yielding

$$\lambda_{eff} = \frac{2}{N}\log\left|\frac{\omega(\alpha,\,1/\alpha)}{\omega(\alpha,\,1/\overline{\alpha})}\right|. \tag{7.18}$$

This is consistent with (1.3) and (4.14) for the $M=1$ case considered by Philip (1972).

The point is that having found the slip length $\lambda_{eff}$ for $M$ menisci in general position around a superhydrophobic pipe, the slip length associated with flow in another pipe where this $M$-menisci pattern is repeated $N$ times around the pipe in a rotationally symmetric pattern is simply $\lambda_{eff}/N$. This quantity clearly decreases with increasing $N$, so there is a deterioration in slip that comes from adding higher-order symmetry in the patterning, a feature that has been noticed elsewhere (Crowdy 2021*b*).

## 8. Discussion

This paper concerns the modelling of a pressure-driven, longitudinal, laminar flow through superhydrophobic pipes, where the aim of the analysis is similar to that of Crowdy (2011), namely to take another solution of Philip's original paper (Philip 1972) and to generalise it to a more diverse class of no-shear surface patterning. It has been shown that the longitudinal flow $(0,\,0,\,w(x,\,y))$ associated with a wide range of superhydrophobic pipes can be written parametrically as

$$w(x,\,y) = \frac{1}{4}\left(1-|z|^2\right) + \log\left|\frac{\omega(\zeta,\,1/\alpha)}{\omega(\zeta,\,1/\overline{\alpha})}\right|, \quad z = x+\mathrm{i}y, \tag{8.1}$$

with

$$z = -\frac{\omega(\zeta, \overline{\alpha})\,\omega(\zeta, 1/\overline{\alpha})}{\omega(\zeta, \alpha)\,\omega(\zeta, 1/\alpha)}, \tag{8.2}$$

where the parametric complex variable $\zeta$ takes values in some upper half circular domain $D_\zeta^+$, and $\omega(\cdot, \cdot)$ is a (generally transcendental) prime function associated with the parametric circular domain $D_\zeta$ made up of $D_\zeta^+$ and its reflection in the real $\zeta$-axis. The domain $D_\zeta^+$, its associated prime function, and the point $\alpha \in D_\zeta^+$ are all determined by the no-shear pattern of the pipe in the manner exemplified in this paper. Moreover, the diagnostic quantity known as the effective slip length associated with these flows is given in terms of the prime function as

$$\lambda_{eff} = 2 \log \left| \frac{\omega(\alpha, 1/\alpha)}{\omega(\alpha, 1/\overline{\alpha})} \right|. \tag{8.3}$$

The prime functions are readily calculated, for example by using freely available MATLAB codes (ACCA 2016). Notice that no square-root branch points appear explicitly in the parametric formulae (8.1) and (8.2). They would, however, appear if the parametric variable $\zeta$ is eliminated between these formulae to find $w(x, y)$ as a function of $(x, y)$. However, except in the $M = 1$ case carried out explicitly in Appendix A, this is not generally possible analytically.

It has been shown explicitly how Philip's solution (1.1)–(1.2) corresponds to $D_\zeta^+$ being the upper half unit $\zeta$ disc, so that $D_\zeta$ is the entire unit $\zeta$ disc with associated prime function $\omega(\zeta, a) = \zeta - a$, and $\alpha = \mathrm{i} \tan(\Phi/4)$, where $\Phi/\pi$ is the no-shear fraction. The analytical expressions derived in this work are a valuable extension of Philip's slippery pipe model (Philip 1972); they permit more flexible geometric configurations to be considered and designed, with the explicit formula for $\lambda_{eff}$ allowing for easier quantification of the associated slip properties.

This paper has considered only menisci having the same curvature as the solid no-slip walls. It may appear that the solutions might be of limited value given that careful pressure control, for example, would be needed to maintain such a situation, and in practice, the menisci might have differing curvatures. However, in the case of channel flow over superhydrophobic surfaces (SHS), it has been shown (Crowdy 2017) how Green's second identity can be used, in conjunction with known exact solutions for flat menisci, to find explicit integral expressions for the leading-order perturbation to the slip length when the menisci are weakly curved, that is, where they are close to the flat state. Earlier, for that same channel flow problem, Sbragaglia & Prosperetti (2007) had carried out a detailed perturbation analysis for weak meniscus curvature to determine the full perturbation problem for the leading-order modififcation to the velocity, but the later analysis of Crowdy (2017) shows this to be unnecessary if only the slip length modification is of interest. By extension, the derivation of similar explicit integral expressions for the modified slip length in a pipe flow should be possible when the curvature of the menisci considered here deviate modestly from that of the no-slip walls. Following Crowdy (2017), deriving such explicit integrals will involve use of integral identities combined with the exact solutions found here.

The new results add to an extensive literature on pressure-driven flow in pipes; the classic monograph by Shah & London (2014), where the principal interest is in quantifying heat transfer diagnostics such as Nusselt numbers, features a comprehensive survey of the many results in this general area. Being a relatively modern concept, superhydrophobic pipes are not a focus of Shah & London (2014), but recent work has shown (Broadbent &

Crowdy 2022) that some, but not all, superhydrophobic pipes allow for an enhancement of the heat transfer properties. This result was unexpected since earlier studies had failed to find any such enhancement (Kirk, Hodes & Papageorgiou 2017) in other flow situations such as channel flows over SHS. This heat transfer application, where details of the geometry of the pipe no-shear patterning is a crucial determinant of performance, shows the value in having available an analytical strategy for solving for flow in more general superhydrophobic pipes with arbitrary no-shear patterning. In particular, the SHS models presented allow for a conceivable scenario in which heat is supplied to the fluid via a larger contiguous solid wall fraction, while lubrication is provided by an array of shear free interfaces situated along the remaining boundary. The design space has therefore been opened up considerably by the solutions herein.

Finally, as mentioned earlier, these solutions (to boundary value problems for Poisson's equation with a constant forcing and mixed Dirichlet-type and Neumann-type boundary conditions) have much broader significance beyond the particular application to slippery pipe flows. Bazant (2016) has identified no less than 17 physical analogies sharing the same mathematical structure as that of pressure-driven pipe flow. The solutions found here are potentially applicable to all those other areas. For example, a recent study by Skvortsov (2020) investigates the so-called mean first-passage time associated with Brownian diffusion of a particle in a planar disc where the boundary has two unequal absorbing regions, the remainder of the boundary being reflecting. That problem is governed by a boundary value problem that is essentially the $M = 2$ scenario of the present paper. Skvortsov (2020) uses a different analytical construction that does not leverage the prime function machinery (Crowdy *et al.* 2016; Crowdy 2020), but the results here for the $M = 2$ case are essentially a rederivation of Skvortsov's solutions within a different function theoretic framework. Moreover, the solutions herein automatically generalise that study to any number of absorbing boundary segments.

In fact, Marshall (2016) had earlier solved the Brownian diffusion problem considered by Skvortsov (2020) using the same prime function machinery used in the present paper, albeit through the lens of potential theory by making an association with so-called Robin's functions. Just as has been done here, Marshall (2016) used the prime functions of higher-connected circular domains (Crowdy *et al.* 2016; Crowdy 2020) to solve the problem for any finite number of absorbing sections, and presented two different representations of the solution, the second of which – see (3.25) of Marshall (2016) – is essentially the solution (8.1). In principle, the present paper could have elucidated the mathematical analogy between pressure-driven pipe flow and the mean first-passage time of Brownian motion, imported the result (3.25) of Marshall's paper, and then used it to calculate the effective slip lengths. However, Marshall (2016) gives only a cursory derivation of his formula (3.25), and his discussion in terms of potential theory is not strictly necessary. The present paper has therefore given an alternative, arguably simpler, geometrical construction of the solutions based on use of conformal slip mappings and directly in the context of the fluid dynamical pipe flow problem, that construction being a natural generalisation of one used by Crowdy (2011) to generalise Philip's solutions for shear flow over SHS. Taken together, the present work and that of Marshall (2016) furnish the reader with several complementary views of this important class of mathematical problems.

It is also worth mentioning that the effective slip lengths calculated here are closely related to global mean first-passage times, which measure the effectiveness of the absorbing boundary of the planar disc at trapping Brownian particles. Marshall (2016) mentions these, but he does not compute them; the effective slip lengths of this paper can thus be reinterpreted as global mean first-passage times in the Brownian motion problem, adding significance to the results in that separate physical application. And these effective

slip length quantities will have analogous importance as global quantifiers in the many other physical contexts set out by Bazant (2016). A final observation is that the extension in § 7 of the present paper to the $N$-fold periodic arrangement with $M$ absorbing sections per sector was not considered by Marshall (2016) and therefore constitutes an extension of those Brownian motion results.

**Funding.** We acknowledge support by the Deutsche Forschungsgemeinschaft (DFG, German Research Foundation), project-ID 467661067. D.G.C. is partially supported by EPSRC grant EP/V062298/1.

**Declaration of interests.** The authors report no conflict of interest.

## Appendix A. Derivation of Philip's form of the single-slot solution

It is instructive to show how to retrieve Philip's formulae (1.1)–(1.2) from the new parametric form of that particular solution derived here. It follows on use of (3.2) and (3.6) in (3.11) that

$$H(\zeta) = \frac{1}{2}\log\left(\frac{\zeta - 1/\alpha}{\zeta - 1/\overline{\alpha}}\right)^2 = \log\left(\frac{1/\alpha - \zeta}{1/\alpha + \zeta}\right), \tag{A1}$$

where the right hand side has been chosen to ensure $\mathrm{Im}[H(\mathrm{i})] = 0$; recall from (3.3) that $\zeta = \mathrm{i}$ is the pre-image of the midpoint of the meniscus. It follows that

$$\frac{1/\alpha - \zeta}{1/\alpha + \zeta} = \mathrm{e}^H, \tag{A2}$$

which can be rearranged to give

$$\zeta = \frac{1}{\alpha}\left(\frac{1 - \mathrm{e}^H}{1 + \mathrm{e}^H}\right). \tag{A3}$$

On taking a logarithm of (3.2), it follows that

$$\log(-z) = \log\left(\frac{\zeta - \alpha}{\zeta + \alpha}\right) + H - \mathrm{i}\pi. \tag{A4}$$

Now introduce

$$\kappa = -\frac{\mathrm{i}}{2}\log z, \quad \text{so that} \quad \log(-z) = 2\mathrm{i}\kappa + \mathrm{i}\pi, \tag{A5}$$

and consequently,

$$2\mathrm{i}\kappa - H + 2\pi\mathrm{i} = \log\left(\frac{\zeta - \alpha}{\zeta + \alpha}\right). \tag{A6}$$

After exponentiation, it follows that

$$\frac{\zeta - \alpha}{\zeta + \alpha} = \mathrm{e}^{2\mathrm{i}\kappa - H}, \tag{A7}$$

which can be rearranged to give

$$\zeta = \alpha\left(\frac{1 + \mathrm{e}^{2\mathrm{i}\kappa - H}}{1 - \mathrm{e}^{2\mathrm{i}\kappa - H}}\right). \tag{A8}$$

The two expressions for $\zeta$ in (A3) and (A8) can now be set equal to eliminate $\zeta$ and provide a relationship between $z$ and $h(z)$:

$$\frac{1}{\alpha}\left(\frac{1-\mathrm{e}^{H}}{1+\mathrm{e}^{H}}\right)=\alpha\left(\frac{1+\mathrm{e}^{2\mathrm{i}\kappa-H}}{1-\mathrm{e}^{2\mathrm{i}\kappa-H}}\right). \tag{A9}$$

It follows that

$$\frac{1}{\alpha^2}=\left(\frac{1+\mathrm{e}^{2\mathrm{i}\kappa-H}}{1-\mathrm{e}^{2\mathrm{i}\kappa-H}}\right)\left(\frac{1+\mathrm{e}^{H}}{1-\mathrm{e}^{H}}\right)=\frac{\cos\kappa+\cos(\kappa+\mathrm{i}H)}{\cos\kappa-\cos(\kappa+\mathrm{i}H)}. \tag{A10}$$

But

$$\frac{1}{\alpha^2}=-\frac{1}{r^2}=-\cot^2(\Phi/4)=-\frac{\cos^2(\Phi/4)}{\sin^2(\Phi/4)}=\frac{\cos(\Phi/2)+1}{\cos(\Phi/2)-1}, \tag{A11}$$

where (3.5) has been used, and familiar trigonometric identities in the last step. On comparison of (A10) and (A11), it is clear that

$$\frac{\cos\kappa}{\cos(\kappa+\mathrm{i}H)}=\cos(\Phi/2),\quad \text{or}\quad \kappa+\mathrm{i}H=\cos^{-1}\left(\frac{\cos\kappa}{\cos(\Phi/2)}\right). \tag{A12}$$

Finally, on taking the imaginary part of this equation to find $H(\zeta)=h(z)$, Philip's formulae (1.1)–(1.2) with $N=1$ are retrieved on substitution of $h(z)$ into (2.4).

## Appendix B. Evaluation of the prime function

Analytical formulae for the solutions have been derived in terms of the prime function $\omega(\cdot,\cdot)$ of a multiply connected circular domain. Given such a circular domain, the most numerically efficient method to compute the associated prime function is to make use of freely available MATLAB codes (ACCA 2016; Crowdy 2020). These codes are based on a numerical algorithm described in detail in Crowdy *et al.* (2016), which extends an earlier one proposed by Crowdy & Marshall (2007).

For a triply connected domain such as that used in § 6, however, it is also known (see Chapter 14 of Crowdy 2020) that the infinite product representation

$$\omega(z,\zeta)=(z-\zeta)\prod_{\Theta\in\Theta''}\frac{(\Theta(z)-\zeta)(\Theta(\zeta)-z)}{(\Theta(z)-z)(\Theta(\zeta)-\zeta)} \tag{B1}$$

is convergent; here, each function $\Theta$ lies in the set of Möbius maps $\Theta''$ that denotes all elements of the free Schottky group generated by the basic Möbius maps

$$\Theta_1(\zeta)\equiv\delta+\frac{q^2\zeta}{1-\delta\zeta},\quad \Theta_2(\zeta)\equiv-\delta+\frac{q^2\zeta}{1+\delta\zeta}, \tag{B2}$$

except for the identity and excluding all inverses (Crowdy & Marshall 2007; Crowdy 2020). For numerical purposes of evaluation, it is necessary to truncate this product, and the natural way to do so is to include all Möbius maps up to a chosen level; see Crowdy & Marshall (2007) and Crowdy (2020) for more details. Use of this infinite product is feasible for most superhydrophobic pipe geometries, but maintaining a required degree of accuracy requires truncation at increasingly high levels as the radii of $C_1$ and $C_2$ get larger, or these circles get close together, and convergence of the product can become unacceptably slow. In such cases, use of the MATLAB code from ACCA (2016) is preferred and advised.

## References


ACCA 2016 Source MATLAB codes. Available at https://github.com/ACCA-Imperial.

Asmolov, E.S., Nizkaya, T.V. & Vinogradova, O.I. 2018 Enhanced slip properties of lubricant-infused grooves. *Phys. Rev. E* **98** (3), 033103.

Bazant, M.Z. 2016 Exact solutions and physical analogies for unidirectional flows. *Phys. Rev. Fluids* **1** (2), 024001.

Belyaev, A.V. & Vinogradova, O.I. 2010 Effective slip in pressure-driven flow past super-hydrophobic stripes. *J. Fluid. Mech.* **652**, 489–499.

Broadbent, H.R. & Crowdy, D.G. 2022 Superhydrophobicity can enhance convective heat transfer in pressure-driven pipe flow. *Q. J. Mech. Appl. Maths* **75** (4), 315–346.

Cassie, A.B.D. & Baxter, S. 1944 Wettability of porous surfaces. *Trans. Faraday Soc.* **40**, 546–551.

Crowdy, D.G. 2010 Slip length for longitudinal shear flow over a dilute periodic mattress of protruding bubbles. *Phys. Fluids* **22** (12), 121703.

Crowdy, D.G. 2011 Frictional slip lengths for unidirectional superhydrophobic grooved surfaces. *Phys. Fluids* **23** (7), 072001.

Crowdy, D.G. 2016 Analytical formulae for longitudinal slip lengths over unidirectional superhydrophobic surfaces with curved menisci. *J. Fluid. Mech.* **791**, R7.

Crowdy, D.G. 2017 Perturbation analysis of subphase gas and meniscus curvature effects for longitudinal flows over superhydrophobic surfaces. *J. Fluid Mech.* **822**, 307–326.

Crowdy, D.G. 2020 Solving Problems in Multiply Connected Domains. SIAM.

Crowdy, D.G. 2021*a* Slip length formulas for longitudinal shear flow over a superhydrophobic grating with partially filled cavities. *J. Fluid. Mech.* **925**, R2.

Crowdy, D.G. 2021*b* Superhydrophobic annular pipes: a theoretical study. *J. Fluid. Mech.* **906**, A15.

Crowdy, D.G., Kropf, E.H., Green, C.C. & Nasser, M. 2016 The Schottky–Klein prime function: a theoretical and computational tool for applications. *IMA J. Appl. Maths* **81** (3), 589–628.

Crowdy, D.G. & Marshall, J.S. 2006 Conformal mappings between canonical multiply connected domains. *Comput. Meth. Funct. Theor.* **6** (1), 59–76.

Crowdy, D.G. & Marshall, J.S. 2007 Computing the Schottky–Klein prime function on the Schottky double of planar domains. *Comput. Meth. Funct. Theor.* **7** (1), 298–308.

Davis, A.M.J. & Lauga, E. 2009 Geometric transition in friction for flow over a bubble mattress. *Phys. Fluids* **21** (1), 011701.

Kirk, T.L., Hodes, M. & Papageorgiou, D.T. 2017 Nusselt numbers for Poiseuille flow over isoflux parallel ridges accounting for meniscus curvature. *J. Fluid Mech.* **811**, 315–349.

Lauga, E. & Stone, H.A. 2003 Effective slip in pressure-driven Stokes flow. *J. Fluid. Mech.* **489**, 55–77.

Liravi, M., Pakzad, H., Moosavi, A. & Nouri-Borujerdi, A. 2020 A comprehensive review on recent advances in superhydrophobic surfaces and their applications for drag reduction. *Prog. Org. Coat.* **140**, 105537.

Marshall, J.S. 2016 Analytical solutions for an escape problem in a disc with an arbitrary distribution of exit holes along its boundary. *J. Stat. Phys.* **165** (5), 920–952.

Philip, J.R. 1972 Flows satisfying mixed no-slip and no-shear conditions. *Z. Angew. Math. Phys.* **23** (3), 353–372.

Rothstein, J.P. 2010 Slip on superhydrophobic surfaces. *Annu. Rev. Fluid Mech.* **42** (1), 89–109.

Sbragaglia, M. & Prosperetti, A. 2007 A note on the effective slip properties for microchannel flows with ultrahydrophobic surfaces. *Phys. Fluids* **19** (4), 043603.

Schnitzer, O. & Yariv, E. 2019 Stokes resistance of a solid cylinder near a superhydrophobic surface. Part 1. Grooves perpendicular to cylinder axis. *J. Fluid. Mech.* **868**, 212–243.

Schönecker, C., Baier, T. & Hardt, S. 2014 Influence of the enclosed fluid on the flow over a microstructured surface in the Cassie state. *J. Fluid. Mech.* **740**, 168–195.

Schönecker, C. & Hardt, S. 2013 Longitudinal and transverse flow over a cavity containing a second immiscible fluid. *J. Fluid. Mech.* **717**, 376–394.

Schönecker, C. & Hardt, S. 2015 Assessment of drag reduction at slippery, topographically structured surfaces. *Microfluid Nanofluid* **19** (1), 199–207.

Shah, R.K. & London, A.L. 2014 *Laminar Flow Forced Convection in Ducts: A Source Book for Compact Heat Exchanger Analytical Data*. Academic Press.

Skvortsov, A. 2020 Mean first passage time for a particle diffusing on a disk with two absorbing traps at the boundary. *Phys. Rev. E* **102** (1), 012123.

Song, D., Song, B., Hu, H., Du, X., Du, P., Choi, C.-H. & Rothstein, J.P. 2018 Effect of a surface tension gradient on the slip flow along a superhydrophobic air–water interface. *Phys. Rev. Fluids* **3** (3), 033303.

TSAI, P., PETERS, A.M., PIRAT, C., WESSLING, M., LAMMERTINK, R. & LOHSE, D. 2009 Quantifying effective slip length over micropatterned hydrophobic surfaces. *Phys. Fluids* **21** (11), 112002.

WANG, D., 2020 Design of robust superhydrophobic surfaces. *Nature* **582** (7810), 55–59.

ZIMMERMANN, S. & SCHÖNECKER, C. 2024 Analytical models for pressure-driven Stokes flow through superhydrophobic and liquid-infused tubes and annular pipes. *J. Fluid. Mech.* **978**, A20.